A Unique Design Approach of Double-Sided LCC Compensated IPT System for Misalignment-Tolerant Characteristic

Xuze Zhang, Jingang Li, and Xiangqian Tong

***Abstract*—For double-sided LCC compensation topology, it is not easy to maintain the output current and output voltage constant over the variation of coupling coefficient and load. Consequently, in this article, a unique design approach is presented. With the presented method, whether during a constant current output procedure or constant voltage output procedure, the resonant frequency maintains constant and cannot be affected by the coupling coefficient and load condition. In addition, the transmission gain is kept constant in different misalignment by the phase shift modulation. Zero voltage switching with the minimum reactive current can be implemented by the switch-controlled capacitor (SCC) regardless of the coupling coefficient and owing to the constant phasor of the current flowing the SCC, the control system of SCC is greatly simplified. Finally, a 60 W prototype is designed to verify the validity of the theoretical analysis. From the results of the experiment, when the coupling coefficient range is between 0.13 and 0.2, the fluctuation factors of output current and output voltage are only 0.5% and 1.0%, respectively.**

***Index Terms*—Double-sided LCC compensation topology, misalignment-tolerant characteristics, phase shift modulation, switch-controlled capacitor (SCC).**

I. Introduction

IN CONTRAST to the traditional physical contact charging approach, inductive power transfer (IPT) technology with unique advantages of stronger environmental adaptability, i.e., highly adaptable to different weather and different environments, nonelectrical connection, and better convenience holds good prospects in many applications, such as underwater devices, implantable medical devices, light rail vehicles, and electric vehicles [1], [2], [3], [4], [5], [6]. However, the misalignment between the transmitting and receiving coils has a serious impact on system performance. On the one hand, charge energy storage devices, such as the lithium-ion battery, are widely employed in these applications. Consequently, to increase the life and cycle duration of these devices, the initial constant current (CC) output procedure and subsequent constant voltage (CV) output procedure must be implemented. Nonetheless, the misalignment causes the output current and the output voltage to fluctuate in both CC and CV output procedures. On the other hand, the misalignment leads to a rise in reactive power and, as a result, a drop in efficiency.

Considerable efforts to solve the above-mentioned issues have been proposed. Several hybrid couplers are adopted to improve misalignment-tolerance [7], [8], [9], [10], [11]. Two auxiliary coils are applied to enhance misalignment performance for constant output current [8]. The use of quadruple-D quadrature pads is proposed to reduce the fluctuation of output voltage, affected by the misalignment [9]. A high misalignment-tolerant characteristic is achieved by coupling a bipolar coupler with a conventional series-series (SS) compensated converter [10]. But additional coils increase the size of the system and reduce the efficiency. Relying on an investigation of the misalignment characteristics of different networks, a few hybrid networks are presented to compensate for the misalignment [12], [13]. In [12], a hybrid SS and S-LCC compensated converter is adopted to achieve CC or CV over the fluctuation of the coupling coefficient. The disadvantage of this hybrid topology is that there is only unidirectional misalignment tolerance. Both CC output and CV output are fulfilled by a novel hybrid network with two auxiliary switches [13]. However, there is low utilization of compensation components. It seems to be a better solution that through rational parameter design, the misalignment-tolerant capability can be improved [14], [15], [16], [17], [18]. In [18], the T-series compensated converter with a novel design method is proposed to maintain constant output current. Nevertheless, only a single CC or CV output can be implemented over the wide range load and misalignment. Through operating the double-sided LCC compensation network at the different resonant frequencies, CC output and CV output can be implemented without any compensation component and additional switch [19], [20], [21]. However, the misalignment of the primary and secondary coils results in the fluctuation of the transmission gain and resonant frequency.

Besides, the misalignment also causes the increase in reactive power. A multivariable control strategy is proposed in [22], which means a model that considers all variables is adopted to improve system efficiency over wide load and misalignment variations. Nevertheless, this strategy is utilized to transmit

Manuscript received 19 April 2022; revised 11 July 2022; accepted 10 August 2022. Date of publication 22 August 2022; date of current version 10 October 2022. Recommended for publication by Associate Editor A. Kuperman. *(Corresponding author: Jingang Li.)*

The authors are with the School of Electrical Engineering, Xi'an University of Technology, Xi'an 710048, China (e-mail: 646652385@qq.com; lijingang@xaut.edu.cn; xqtong@xaut.edu.cn).

Color versions of one or more figures in this article are available at https://doi.org/10.1109/TPEL.2022.3200719.

Digital Object Identifier 10.1109/TPEL.2022.3200719

target power and does not take into account CC and CV output. Several different impedance matching networks are employed to compensate for misalignment [23], [24], [25], [26], [27], [28], [29]. In [23] and [24], the capacitance matrix and multiorder L-type matching circuit are used, respectively, where the compensating elements are switched by controlling the auxiliary switch. However, this method results in low utilization of the compensation elements and increases the size and cost of the system. A variable inductor is adopted to regulate the impedance of the SS network [25]. However, a complex control strategy must be adopted to adjust the variable inductor, which increases the complexity of the control system. Adopting SCC seems to be an efficient impedance matching method for compensating reactive power [26], [27], [28], [29]. With the SCC, the CC and CV output procedures of the series/series-parallel network are implemented over the wide misalignment [26]. Unfortunately, the resonant frequency in the CC output procedure depends on the coupling coefficient, which means that the identification of coupling coefficients is required. In [28] and [29], through adopting the SCC, the inductor-capacitor-capacitor-series and double-sided LCC compensated IPT system implement zero voltage switching (ZVS) of CC output procedure and CV output procedure, respectively. However, only a single CC or CV output can be implemented. Besides, the phasors of the resonant current, which is affected by the misalignment, have to be detected to generate the correct driver signals for ensuring that the SCC can operate properly.

In this article, for double-sided LCC compensation topology, a unique design method with a switch-controlled capacitor (SCC) and phase shift modulation is presented to compensate for misalignment between the primary and secondary coils for charging energy storage devices. The proposed method offers the following advantages over the previous method.

1) In both CC and CV output procedures, with the presented parameter design method, the resonant frequency is constant regardless of the misalignment and the output current/voltage is unaffected by the load. This means that compared to other methods, the influence caused by the load variation and misalignment is lowered.
2) With the SCC, ZVS for reactive current minimization is implemented in two modes. Further, the phase of the current flowing through the SCC is unaffected by the load or the coupling coefficient, which means that the SCC can be adopted without any phase detection circuit of current.
3) In the absence of any complicated control technique, conventional phase shift control is applied to compensate for deviations in output current or voltage, caused by the misalignment between the primary coil and the secondary coil. In addition, two output procedures can be achieved at different constant frequencies. This means that the complexity of the control system is greatly reduced.

Additionally, the other parts of this article are composed as indicated below: in Section II, the resonant conditions for the CC and CV output procedures, as well as the impedance analysis of the suggested circuit are described in this article. Section III presents several principles for the control logic and gives the design procedure of the proposed method. The results of the simulation and experimental platform are revealed in Section IV. Finally, Section V derives several conclusions.

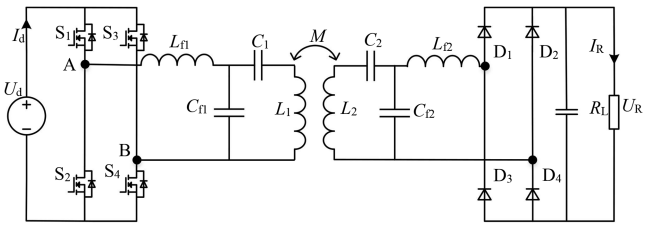

Fig. 1. Double-sided LCC compensation network.

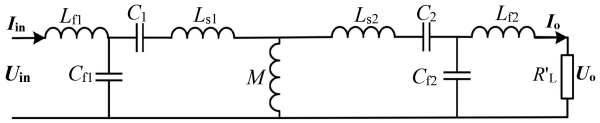

Fig. 2. Leakage inductance equivalent model of double-sided LCC compensation topology.

II. Analysis of Characteristics for Double-Sided LCC Compensation Network

Fig. 1 depicts the double-sided LCC compensation network. L_1, L_2, and M denote self-inductance of the coils at the transmitter and receiver and mutual inductance, respectively. The transmitter compensation circuit is made up of L_{f1}, C_{f1}, and C_1, whereas the receiver compensation circuit is formed by L_{f2}, C_{f2}, and C_2. R_L is the load. The load voltage and current are represented by U_R and I_R, respectively. The high-frequency inverter, which consists of four MOSFETs $S_{1,23,4}$, can drive the input dc voltage U_d. The full-bridge uncontrolled rectifier is formed by the four Schottky diodes.

Fig. 2 depicts the leakage equivalent circuit. L_{s1} and L_{s2} is the leakage inductance of the coils at the transmitting and receiving side. R'_L is the equivalent load. U_{in}, I_{in}, U_o, and I_o are the root-mean-square values of the input voltage, input current, the current, and voltage of the equivalent load R'_L. $\boldsymbol{U_{in}}$, $\boldsymbol{I_{in}}$, $\boldsymbol{U_o}$, and $\boldsymbol{I_o}$ indicate the phasors of corresponding variables.

The individual components and input impedance of the leakage inductance equivalent model can be expressed as (1) and (2)

$$\begin{aligned} L_{s1} &= L_1 - M \qquad k = \frac{M}{\sqrt{L_1 L_2}} \\ L_{s2} &= L_2 - M \qquad R'_L = \frac{8R_L}{\pi^2} \end{aligned} \tag{1}$$

$$Z_{in} = j\omega L_{f1} + \frac{1}{j\omega C_{f1}} // \left(j\omega A + Z // j\omega M\right) \tag{2}$$

where k denotes the coupling coefficient, $Z = j\omega B + [1/j\omega C_{f2} // (R'_L + j\,\omega L_{f2})]$, $A = L_{s1}\text{-}1/\omega^2 C_1$, and $B = L_{s2}\text{-}1/\omega^2 C_2$.

A. Equivalent Model Analysis

There are many equivalent model methods of the double-sided LCC compensation circuit to achieve CC and CV over the wide load range [19], [20], [21]. However, the resonant frequency in the CC or CV output procedure established by these equivalent

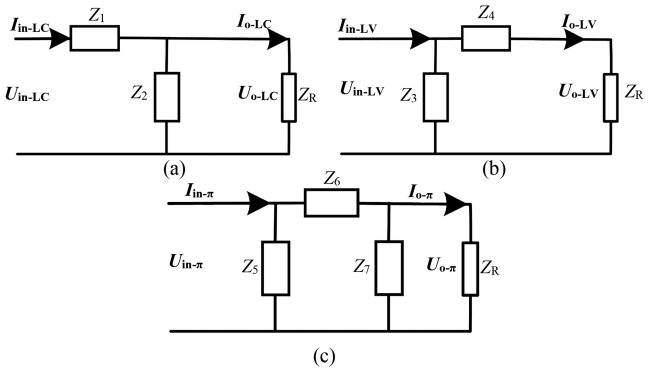

Fig. 3. Equivalent model. (a) Voltage-fed L-circuit. (b) Current-fed L-circuit. (c) Current-fed π-circuit.

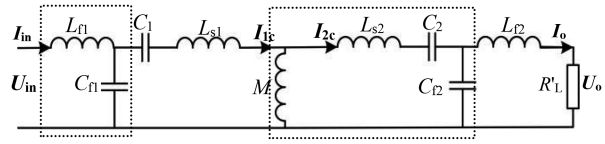

Fig. 4. Leakage inductance equivalent model for CC mode.

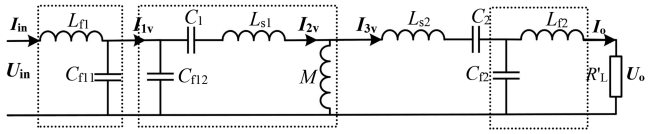

Fig. 5. Leakage inductance equivalent model for CV mode.

approaches may be changed, if the misalignment varies. As a result, in this article, a hybrid equivalent model of the L-network and π-network, as shown in Fig. 3, is adopted to achieve constant resonant frequency in both CC and CV output procedures independent of the misalignment. $Z_1, Z_2, Z_3, Z_4, Z_5, Z_6$, and Z_7 are the equivalent impedances of the corresponding components in Fig. 3. $\boldsymbol{U}_{\mathbf{in\text{-}LV}}, \boldsymbol{I}_{\mathbf{in\text{-}LV}}, \boldsymbol{U}_{\mathbf{in\text{-}LC}}, \boldsymbol{I}_{\mathbf{in\text{-}LC}}, \boldsymbol{U}_{\mathbf{in\text{-}}\pi}, \boldsymbol{I}_{\mathbf{in\text{-}}\pi}, \boldsymbol{U}_{\mathbf{o\text{-}LV}}$, $\boldsymbol{I}_{\mathbf{o\text{-}LV}}$, $\boldsymbol{U}_{\mathbf{o\text{-}LC}}$, $\boldsymbol{I}_{\mathbf{o\text{-}LC}}$, $\boldsymbol{U}_{\mathbf{o\text{-}}\pi}$, and $\boldsymbol{I}_{\mathbf{o\text{-}}\pi}$ indicate the phasors of input voltage, input current, output voltage, and output current in different circuits, respectively.

It can be derived from Fig. 3(a) that the output current $\boldsymbol{I}_{\mathbf{o\text{-}LC}}$ can be expressed as

$$\boldsymbol{I}_{\mathrm{o}-LC} = \frac{Z_2}{(Z_1+Z_2)\,Z_{\mathrm{R}} + Z_1 Z_2}\boldsymbol{U}_{in-LC}. \tag{3}$$

As can be noticed from (3), if the condition in (4) is satisfied by designing Z_1 and Z_2, the output current, whose value and phase are independent of the load Z_{R}, can be represented as (5)

$$Z_1 + Z_2 = 0 \tag{4}$$

$$\boldsymbol{I}_{\mathrm{o}-LC} = \frac{\boldsymbol{U}_{in-LC}}{Z_1}. \tag{5}$$

Similarly, several conclusions can be drawn from the network shown in Fig. 3(b) and (c). If Z_3, Z_4, Z_5, Z_6, and Z_7 meet the criteria in (6) and (7), respectively, the load-independent characteristic of output voltage $\boldsymbol{U}_{\mathbf{o\text{-}LV}}$ and output current $\boldsymbol{I}_{\mathbf{o\text{-}}\pi}$, expressed as (8) and (9), is implemented

$$Z_3 + Z_4 = 0 \tag{6}$$

$$Z_5 + Z_6 + Z_7 = 0 \tag{7}$$

$$\mathrm{U}_{\mathrm{o-LV}} = Z_3 \boldsymbol{I}_{in-LC} \tag{8}$$

$$\boldsymbol{I}_{o-\boldsymbol{\pi}} = -\frac{Z_5}{Z_7}\boldsymbol{I}_{in-\boldsymbol{\pi}}. \tag{9}$$

B. Implementation of CC and CV Output Procedures

Based on the analysis of several models above, it is clear from Fig. 2 that the resonant frequency can maintain constant unaffected by the coupling coefficient and the load, if the equivalent model contains the mutual inductance *M* and does not contain the load *R*'$_{\mathrm{L}}$. As illustrated in Fig. 4, the double-sided LCC leakage model can be equated to a combination of a voltage-fed L-circuit and a current-fed π-circuit. It can be derived from (4)–(6), and (8) that the resonant condition and output current can be represented as

$$\omega_{\mathrm{c}}^2 = \frac{1}{L_{\mathrm{f1}}C_{\mathrm{f1}}} = \frac{1}{L_2}\left(\frac{1}{C_{\mathrm{f2}}} + \frac{1}{C_2}\right) \tag{10}$$

$$\boldsymbol{I}_{\mathrm{o}-c} = \omega_{\mathrm{c}}^2 k\sqrt{L_1 L_2}C_{\mathrm{f2}}\boldsymbol{I}_{1\mathrm{c}} = \frac{\omega_{\mathrm{c}} k\sqrt{L_1 L_2}C_{\mathrm{f2}}\boldsymbol{U}_{\mathrm{in}}}{jL_{\mathrm{f1}}}. \tag{11}$$

As shown in (10), neither coupling coefficient nor load can affect the resonant frequency, i.e., the system can be operated at a constant frequency in the CC output procedure. The output current is independent of the load, according to (11).

Fig. 4 can be equated to Fig. 5 for deriving CV conditions. Where C_{f11} and C_{f12} can be expressed as

$$C_{\mathrm{f11}} + C_{\mathrm{f12}} = C_{\mathrm{f1}}. \tag{12}$$

As shown in Fig. 5, the leakage model can be equated to a combination of a voltage-fed L-circuit, a current-fed π-circuit, and a current-fed L-circuit. Based on (4)–(9), the resonant condition and output voltage can be expressed as (13) and (14)

$$\omega_{\mathrm{v}}^2 = \frac{1}{L_{\mathrm{f1}}C_{\mathrm{f11}}} = \frac{1}{L_1}\left(\frac{1}{C_{\mathrm{f12}}} + \frac{1}{C_1}\right) = \frac{1}{L_{\mathrm{f2}}C_{\mathrm{f2}}} \tag{13}$$

$$\begin{aligned}\boldsymbol{U}_{\mathrm{o}-v} &= \frac{\boldsymbol{I}_{3\mathrm{v}}}{j\omega_{\mathrm{v}}C_{\mathrm{f2}}} = \frac{\boldsymbol{I}_{2\mathrm{v}}}{j\omega_{\mathrm{v}}^3 C_{\mathrm{f2}}C_{\mathrm{f12}}k\sqrt{L_1 L_2}} \\ &= \frac{-\boldsymbol{U}_{in}}{\omega_{\mathrm{v}}^4 C_{\mathrm{f2}}k\sqrt{L_1 L_2}L_{\mathrm{f1}}C_{\mathrm{f12}}}.\end{aligned} \tag{14}$$

Likewise, according to (13) and (14), the resonant frequency can not be affected by the coupling coefficient and the output voltage is constant regardless of the load.

It is clear from the above analysis that in both CC and CV output procedures, the load does not affect either the output voltage/current or the resonant frequency and the coupling coefficient has no effect on the resonant frequency. This means that for the presented system, different constant operating frequencies are implemented in CC and CV output procedures, which greatly simplifies the complexity of system control. However, the misalignment can affect the output current and voltage from

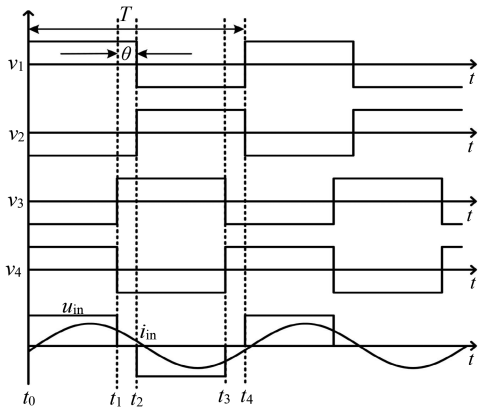

Fig. 6. Switching sequence of phase-shifted control.

(11) and (14). To solve this issue, the conventional phase shift modulation strategy is adopted.

Fig. 6 depicts the typical operating waveforms of the phase shift modulation, where $v_{1,23,4}$ denote the drive signals of four MOSFETs. In addition, T and θ denote the operating period and phase shift angle, respectively. The root-mean-square values of the input voltage U_{in}, is given as

$$U_{\text{in}} = \frac{2\sqrt{2}U_{\text{d}}}{\pi}\cos\frac{\theta}{2}. \tag{15}$$

Substituting (15) into (11) and (14), respectively, the output current $I_{\text{o-c}}$ in CC procedure and the output voltage $U_{\text{o-v}}$ in CV procedure can be denoted as (16) and (17). As a result, it can be observed that the variation of $I_{\text{o-c}}$ and $U_{\text{o-v}}$, caused by the misalignment, can be compensated for by adjusting the phase shift angle θ

$$I_{\text{o-c}} = \frac{2\sqrt{2}\omega_{\text{c}}k\sqrt{L_1L_2}C_{\text{f2}}U_{\text{d}}}{\pi L_{\text{f1}}}\cos\frac{\theta}{2} \tag{16}$$

$$U_{\text{o-v}} = \frac{2\sqrt{2}U_{\text{d}}}{\pi\omega_{\text{v}}^4 C_{\text{f2}}k\sqrt{L_1L_2}L_{\text{f1}}C_{\text{f12}}}\cos\frac{\theta}{2}. \tag{17}$$

C. Implementation of ZVS

Based on the previous section, the CC and CV output procedures can be realized only by conventional phase shift modulation over the variation of coupling coefficient and load. However, variations of the coupling coefficient can affect the input impedance, resulting in a reduction in efficiency.

Therefore, it is necessary to derive the impedance in both output procedures to analyze the effect of the misalignment between the coils at the transmitter and receiver. By substituting (10) and (13) into (2), respectively, the impedance $Z_{\text{in-c}}$ and $Z_{\text{in-v}}$ in CC and CV output procedures can be deduced as (18) and (19)

$$Z_{\text{in-c}} = \frac{L_{\text{f1}}\left(A_{\text{c}} + jB_{\text{c}}\right)}{C_{\text{f1}}\left(A_{\text{c}}^2 + B_{\text{c}}^2\right)} \tag{18}$$

$$Z_{\text{in-v}} = \frac{\omega_{\text{v}}^4 C_{\text{f12}}^2 k^2 L_1L_2L_{\text{f1}}\left(A_{\text{v}} + jB_{\text{v}}\right)}{C_{\text{f1}}\left(A_{\text{v}}^2 + B_{\text{v}}^2\right)} \tag{19}$$

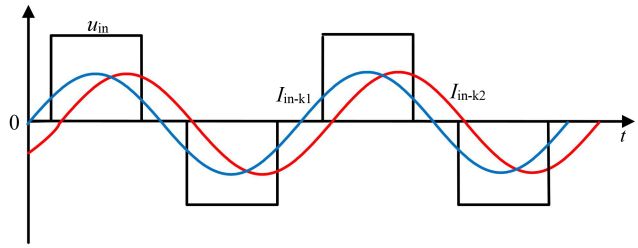

Fig. 7. Typical output waveforms of the phase shift modulation.

where A_{c}, B_{c}, A_{v}, and B_{v} can be expressed as

$$\begin{aligned}
A_{\text{c}} &= \omega_{\text{c}}^4 C_{\text{f2}}^2 k^2 L_1L_2R'_{\text{L}} \\
B_{\text{c}} &= \omega_{\text{c}}^3 C_{\text{f2}}k^2L_1L_2 - \omega_{\text{c}}^5 k^2 L_1L_2C_{\text{f2}}^2L_{\text{f2}} - \omega_{\text{c}}L_1 + \tfrac{1}{\omega_{\text{c}}C_1} + \tfrac{1}{\omega_{\text{c}}C_{\text{f1}}} \\
A_{\text{v}} &= \tfrac{L_{\text{f2}}}{R'_{\text{L}}C_{\text{f2}}} \\
B_{\text{v}} &= \omega_{\text{v}}L_2 - \tfrac{1}{\omega_{\text{v}}C_2} - \tfrac{1}{\omega_{\text{v}}C_{\text{f2}}} - \omega_{\text{v}}^3 C_{\text{f12}}^2 k^2 L_1L_2\left(\tfrac{1}{C_{\text{f11}}} + \tfrac{1}{C_{\text{f12}}}\right).
\end{aligned} \tag{20}$$

It can be concluded from (18) and (19) that if the coupling coefficient satisfies the condition in (21) and (22), i.e., $B_{\text{c}} = 0$ and $B_{\text{v}} = 0$, the input impedance angle is equal to 0 in CC and CV output procedures. At this point, with the coupling coefficient increasing in both output procedures, the imaginary part is greater than zero, and on the contrary less than zero. Besides, the phase shift modulation may prevent the MOSFET from achieving soft switching. Therefore, the impedance modifying technology must be adopted to compensate for the efficiency reduction caused by the misalignment

$$k_{\text{c}}^2 = \frac{\omega_{\text{c}}^2 L_1 - \frac{1}{C_1} - \frac{1}{C_{\text{f1}}}}{\omega_{\text{c}}^4 C_{\text{f2}}L_1L_2\left(1 - \omega_{\text{c}}^2 L_{\text{f2}}C_{\text{f2}}\right)} \tag{21}$$

$$k_{\text{v}}^2 = \frac{\omega_{\text{v}}^2 L_2 - \frac{1}{C_{\text{f2}}} - \frac{1}{C_2}}{\omega_{\text{v}}^4 C_{\text{f12}}^2 L_1L_2\left(\frac{1}{C_{\text{f11}}} + \frac{1}{C_{\text{f12}}}\right)} \tag{22}$$

Based on (10), (11), and (18), in the CC output procedure, the impedance can be adjusted by changing the compensation capacitor C_1, which has no effect on either the resonant frequency or the output current. A similar conclusion can be deduced from (13), (14), and (19). The compensation capacitor C_2 in the CV output procedure can perform the same function as the compensation components C_1 in the CC output procedure.

For a converter containing MOSFETs and diodes, ZVS is favored over zero current soft switching [30]. As a result, for the implementation of ZVS, the correct analysis about the turn-OFF current to meet the condition in (23) is a critical element [30]

$$I_{\text{pk}} \geq \frac{2U_{\text{bus}}C_{\text{j}}}{t_{\text{dead}}} \tag{23}$$

where I_{pk}, U_{b}, C_{j}, and t_{d} denote the turn-OFF peak current, input voltage, parasitic capacitor, and dead time of MOSFET, respectively.

According to the above-mentioned analysis, when the phase shift modulation is adopted, typical output waveforms at different coupling coefficients are shown in Fig. 7. From Fig. 7, the turn-OFF peak current of MOSFETs may be positive, i.e., ZVS is not implemented when the misalignment occurs. Consequently,

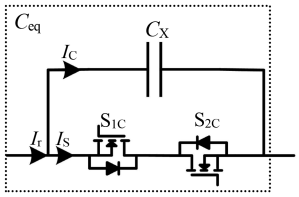

Fig. 8. Circuit diagram of SCC.

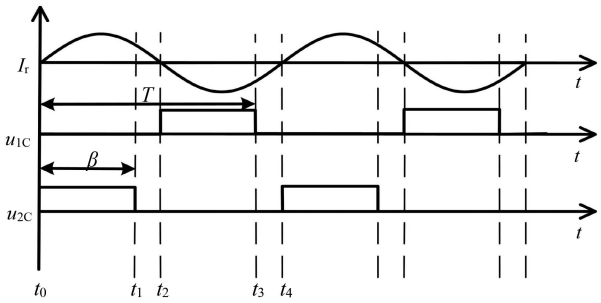

Fig. 9. Typical operation waveforms of SCC.

it is necessary to regulate the input impedance for the achievement of ZVS.

According to Fig. 6, the turn-OFF current $i_c(t_0)$ in the CC output procedure and $i_v(t_0)$ in the CV output procedure can be deduced from (18) and (19) and represented as

$$i_{\mathrm{c}}\left(\mathrm{t}_0\right)=\frac{4C_{\mathrm{f1}}U_{\mathrm{d}}}{\pi L_{\mathrm{f1}}}\cos\frac{\theta}{2}\sqrt{A_{\mathrm{c}}^2+B_{\mathrm{c}}^2}\sin\left(\frac{\theta}{2}-\alpha_{\mathrm{c}}\right) \tag{24}$$

$$i_{\mathrm{v}}\left(\mathrm{t}_0\right)=\frac{4C_{\mathrm{f1}}U_{\mathrm{d}}}{\pi L_{\mathrm{f1}}\omega_{\mathrm{v}}^4C_{\mathrm{f12}}^2k^2L_1L_2}\cos\frac{\theta}{2}\sqrt{A_{\mathrm{v}}^2+B_{\mathrm{v}}^2}\sin\left(\frac{\theta}{2}-\alpha_{\mathrm{v}}\right) \tag{25}$$

where α_c and α_v are represented as

$$\begin{aligned}\alpha_{\mathrm{c}}&=\arctan\left(B_{\mathrm{c}}/A_{\mathrm{c}}\right)\\ \alpha_{\mathrm{v}}&=\arctan\left(B_{\mathrm{v}}/A_{\mathrm{v}}\right).\end{aligned} \tag{26}$$

It is clear from the above-mentioned analysis in this section that ZVS can be achieved in the CC output procedure by modifying C_1 to fulfill the condition in (27), and in the CV output procedure, by adjusting C_2 to satisfy the condition in (28)

$$-i_{\mathrm{c}}\left(t_0\right)=I_{\mathrm{pk}}\geq\frac{2U_{\mathrm{bus}}C_{\mathrm{j}}}{t_{\mathrm{dead}}} \tag{27}$$

$$-i_{\mathrm{v}}\left(t_0\right)=I_{\mathrm{pk}}\geq\frac{2U_{\mathrm{bus}}C_{\mathrm{j}}}{t_{\mathrm{dead}}}. \tag{28}$$

There are several impedance adjustment techniques [23], [24], [25], [26], [27], [28], [29]. For the capacitance matrix [23], it results in low utilization of the compensation elements and increases the size and cost of the system. For the variable inductor [25], magnetic saturation problems may occur. Consequently, compared to other impedance adjustment techniques, the SCC, represented in Fig. 8, is a very effective strategy [26], [27], [28], [29]. The typical operating waveform of the SCC is depicted in Fig. 9, where C_{eq} is the equivalent capacitance of SCC, while u_{1C} and u_{2C} are the drive signals of S_{1C} and S_{2C}. At the positive half-cycle of the current I_r, maintaining S_{1C} OFF, the capacitor C_x is discharged under the condition that S_{2C} is ON, while charged under the condition that S_{2C} is OFF. At the negative half-cycle of the current I_r, maintaining S_{2C} OFF, the capacitor C_x is discharged under the condition that S_{1C} is ON, while charged under the condition that S_{2C} is OFF. As a result, by adjusting the associated control angle β ($\pi/2<\beta<\pi$), C_{eq} can be regulated and represented as

$$C_{\mathrm{eq}}=\frac{\pi C_{\mathrm{x}}}{2\pi-2\beta+\sin\left(2\beta\right)}. \tag{29}$$

The main distinguishing characteristic of the SCC, as shown in Fig. 9, is that the driver signals of S_{1C} and S_{2C} must be generated based on the phasor of the current I_r. Based on (11) and (14), the current $\boldsymbol{I_{1c}}$ and $\boldsymbol{I_{2v}}$ can be calculated as

$$\boldsymbol{I}_{1\mathrm{c}}=\frac{\boldsymbol{U}_{\mathrm{in}}}{j\omega_{\mathrm{c}}L_{\mathrm{f1}}} \tag{30}$$

$$\boldsymbol{I}_{2\mathrm{v}}=\frac{\boldsymbol{U}_{in}}{j\omega_{\mathrm{v}}^3L_{\mathrm{f1}}C_{\mathrm{f12}}k\sqrt{L_1L_2}}. \tag{31}$$

It can be deduced from (30) and (31) that the phasors of $\boldsymbol{I_{1c}}$ and $\boldsymbol{I_{2v}}$, which are irrelevant of load and coupling coefficient, remain constant and always lag 90° behind the input voltage. This means that without the phase detection device, the SCC can be adopted to match the impedance in two output procedures with the proposed method. Consequently, in this article, C_1 and C_2 can be respectively contacted by an SCC in series to adjust the impedance in CC and CV output procedures.

D. Analysis of Power Losses

In the proposed IPT system, the power losses are mainly composed of four parts, i.e., the losses of four rectifier diodes, the resonant circuit, two SCCs, and four inverter MOSFETs [28].

According to [28], the losses of rectifier diodes can be calculated as follows:

$$P_{\mathrm{d-loss}}=\frac{2\sqrt{2}V_{\mathrm{f}}I_{\mathrm{o}}}{\pi}+I_{\mathrm{o}}^2r_{\mathrm{d}}. \tag{32}$$

where the forward voltage drop and the on-state resistance are expressed by V_f and r_d.

Likewise, the power losses about the resonant circuit consisting of the equivalent series resistances of transmitting coil, receiving coil, and compensation components, can be expressed as [28]

$$\begin{aligned}P_{\mathrm{lc-loss}}=&I_{\mathrm{Lf1}}^2r_{\mathrm{Lf1}}+I_{\mathrm{Cf1}}^2r_{\mathrm{Cf1}}+I_{\mathrm{L1}}^2\left(r_{\mathrm{C1}}+r_{\mathrm{L1}}\right)\\&+I_{\mathrm{L2}}^2\left(r_{\mathrm{C2}}+r_{\mathrm{L2}}\right)+I_{\mathrm{Lf2}}^2r_{\mathrm{Lf2}}+I_{\mathrm{Cf2}}^2r_{\mathrm{Cf2}}\end{aligned} \tag{33}$$

where I_{Lf1}, I_{Cf1}, I_{L1}, I_{L2}, I_{Lf2}, I_{Cf2} express the current flowing through the corresponding components and r_{Lf1}, r_{Cf1}, r_{C1}, r_{L1}, r_{L2}, r_{C2}, r_{Lf2}, r_{Cf2} represent equivalent resistances of the corresponding components.

The power losses of the inverter MOSFETs mainly include conduction losses and switching losses [28]. Due to the implementation of ZVS, switching losses are greatly reduced. The conduction losses are derived as

$$P_{\mathrm{on-loss}}=\frac{I_{\mathrm{in}}^2r_{\mathrm{ds}}}{\pi}\left(3\pi-\theta-\sin\theta\right) \tag{34}$$

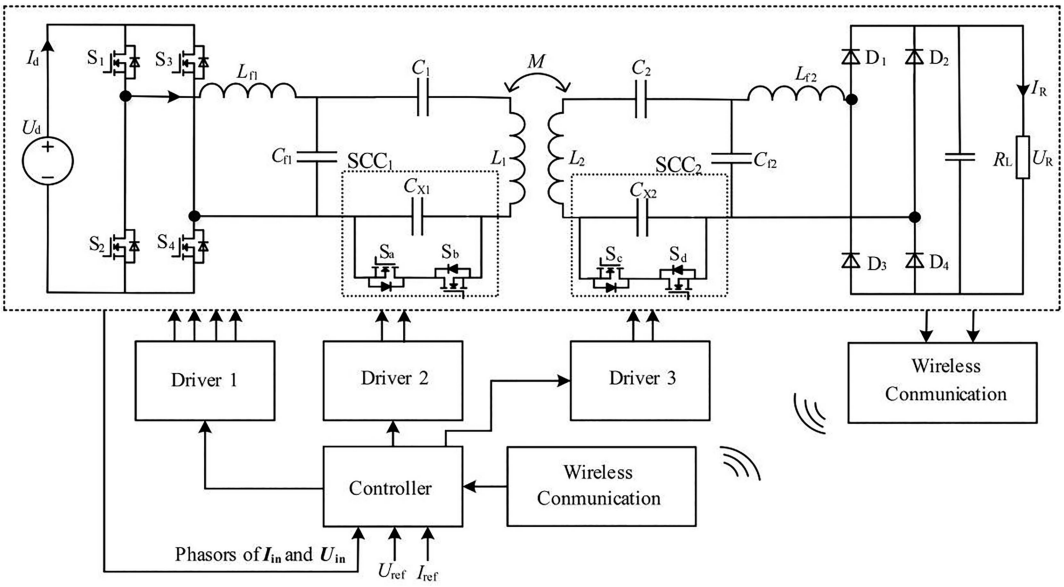

Fig. 10. Schematic diagram of the proposed WPT system.

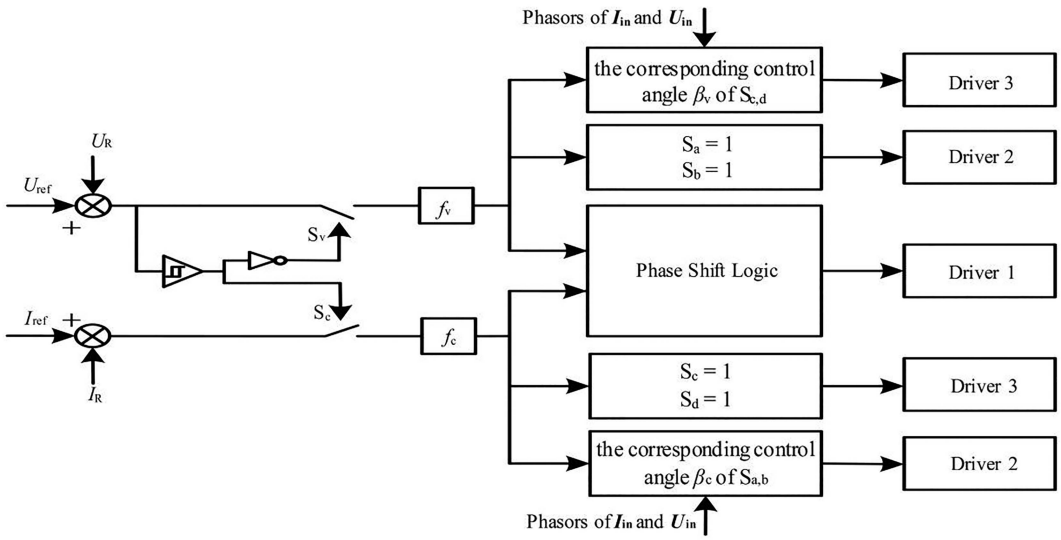

Fig. 11. Schematic of control logic for the IPT charger.

where r_{ds} is the on-state resistance of the MOSFET.

According to [28], the losses of the SCC is expressed as

$$P_{\mathrm{SCC-loss}} = I_S^2 r_{ds} + I_C^2 r_C \tag{35}$$

where r_C represents the equivalent resistance of C_X.

II. Implementation of the Presented IPT System

A. Analysis and Design of the Control System

Based on the schematic illustration of the presented IPT system represented in Fig. 10, the feedback signals consist of the load voltage U_R, load current I_R, and the phasor of $\boldsymbol{U_{in}}$ and $\boldsymbol{I_{in}}$. The feedback signals are transmitted to the controller to enable Driver 1, Driver 2, and Driver 3 modules for generating the driver signals of MOSFETs $S_{1,23,4,a,b,c,d}$ to implement the constant output and ZVS in two procedures.

The control logic of the controller is shown in Fig. 11. The first step is to compare the load voltage with the reference value to determine whether the system should be operated in CC output procedure, i.e., $S_v = 0$ and $S_c = 1$ or CV output procedure, i.e., $S_v = 1$ and $S_c = 0$. Then, the switching logic of the MOSFETs generated by the conventional phase-shift control is transmitted to Driver 1. In addition, in the CV output procedure, the MOSFETs $S_{a,b}$ maintain ON to eliminate alteration of the resonant frequency caused by C_{X1}, while the associated control angle β_v of $S_{c,d}$ are generated based on the phasors of $\boldsymbol{I_{in}}$ and $\boldsymbol{U_{in}}$, i.e., $\beta_v = \beta_v$ - $\Delta\beta_v$, when the phase displacement between $\boldsymbol{I_{in}}$ and $\boldsymbol{U_{in}}$ is less than zero, and $\beta_v = \beta_v + \Delta\beta_v$, when the phase displacement between $\boldsymbol{I_{in}}$ and $\boldsymbol{U_{in}}$ is greater than zero.

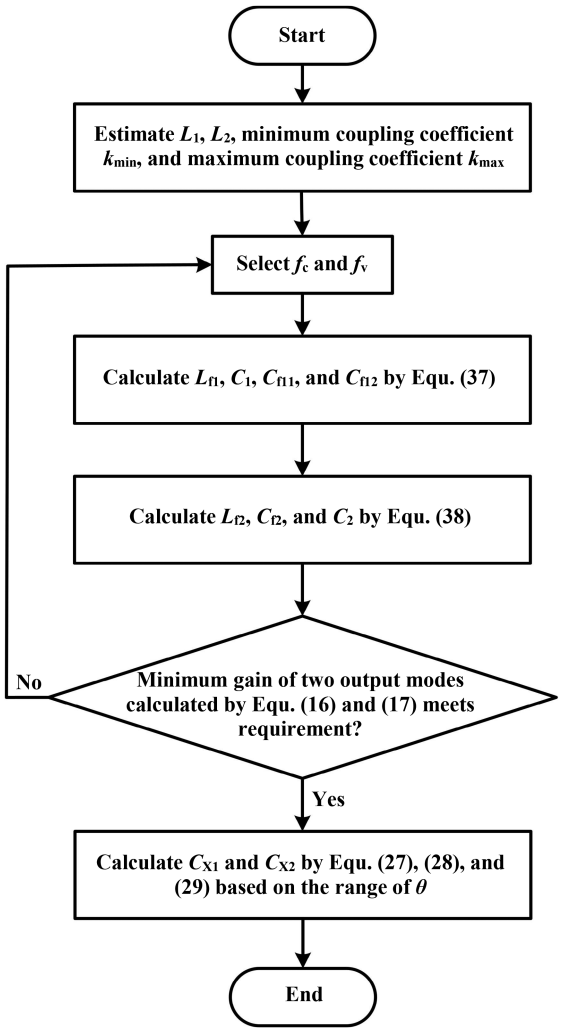

Fig. 12. Design procedure of the proposed double-sided LCC IPT converter.

In the CC output procedure, the associated control angle β_c of $S_{a,b}$ are generated based on the phasor of $\boldsymbol{I}_{in}$ and $\boldsymbol{U}_{in}$, i.e., $\beta_c = \beta_c - \Delta\beta_c$, when the phase displacement between $\boldsymbol{I}_{in}$ and $\boldsymbol{U}_{in}$ is less than zero, and $\beta_c = \beta_c + \Delta\beta_c$, when the phase displacement between $\boldsymbol{I}_{in}$ and $\boldsymbol{U}_{in}$ is greater than zero, while MOSFETs $S_{c,d}$ maintain ON to achieve the same purpose as the CC output procedure.

B. Parametric Analysis and Design Procedure

According to the previous analysis, a set of parameters are required in the practical application to satisfy the condition that the output current/voltage is independent of the load and the resonant frequency is irrelevant to the coupling coefficient. As a result, the actual design process is presented in Fig. 12 for the implementation of the proposed system.

First of all, the self-inductances of the coils at the transmitter and receiver need to be estimated by considering the volume of the practical system. In addition, the minimum and maximum coupling coefficient k_{min} and k_{max} should be determined based on air gap and maximum misalignment between two coils to ensure safe system operation. In the next step, resonant frequencies at CC and CV output procedures should be selected based on the volume of the compensation components. According to the analysis in the previous section, resonant frequencies f_v and f_c at CC and CV output procedures should be selected to satisfy the condition in (36). In general, the operating frequency of IPT systems is selected between 20 and 95 kHz [19], [20]. Thus, the resonant frequencies of CC and CV output procedures could be selected as 81 and 90 kHz, respectively. Then, according to the above analysis the compensation element parameters are designed under the assumption that $k = k_{max}$. Consequently, it can be deduced from (10), (12), and (13) that the value for L_{f1}, C_{f1}, C_{f11}, C_{f12}, and C_1 can be calculated by using (37). Furthermore, from (21) and (22), C_2, C_{f2}, and L_{f2} can be determined by (38)

$$\frac{f_c}{f_v} \geq \sqrt{1-k} \tag{36}$$

$$\begin{aligned} L_{f1} &= \frac{\omega_v^4 k L_1}{\omega_c^4} C_{f1} = \frac{1}{\omega_c^4 L_{f1}} C_{f11} = \frac{1}{\omega_v^4 L_{f1}} \\ C_{f12} &= \frac{\omega_v^2 - \omega_c^2}{L_{f1}\omega_c^2\omega_v^2} C_1 = \frac{C_{f12}}{\omega_v^2 L_1 C_{f12} - 1} \end{aligned} \tag{37}$$

$$\begin{aligned} L_{f2} &= \frac{\omega_c^4 k^2 L_1 L_2 C_{f1} C_1 \left(\omega_v^2 - \omega_c^2\right)}{\omega_v^4 \left(\omega_c^2 L_1 C_{f1} C_1 - C_1 - C_{f1}\right)} \\ C_{f2} &= \frac{1}{\omega_v^2 L_{f2}} C_2 = \frac{C_{f2}}{\omega_c^2 L_2 C_{f2} - 1}. \end{aligned} \tag{38}$$

At this point, it is indispensable to check whether minimum transmission gains calculated by (16) and (17) in two output procedures, i.e., assuming $k = k_{min}$ in CC output procedure and assuming $k = k_{max}$ in CV output procedure, meet electrical specifications of the system. If the results are not satisfied, the resonant frequencies need to be reselected. Substitute (37) and (38) into (16) and (17), transmission gains g_c and g_v in two output procedures can be expressed as (39) and (40). It can be noticed from (39) and (40) that transmission gains g_c and g_v essentially increase with the f_c. Next step, C_{X1} and C_{X2} need be calculated to implement ZVS with minimum reactive current. Based on (29), the equivalent capacitance of SCC increases with the associated control angle β. Consequently, the minimum value of SCC_1 and SCC_2 should be calculated and equal to C_{X1} and C_{X2}. Based on the analysis in the previous section, C_{X1} can be calculated by using (27) and (29) assuming $k = k_{max}$ in CC output procedure and C_{X2} can be calculated by using (28) and (29) assuming $k = k_{mim}$ in CV output procedure

$$g_c = \frac{2\sqrt{2}\omega_c}{\pi k\sqrt{L_1 L_2}\omega_v^2}\cos\frac{\theta}{2}\left(\frac{\omega_v^6 k^2 L_1}{\omega_v^2 - \omega_c^2} - \frac{\omega_v^4 k^2 L_1}{\omega_c^2} - \omega_v^2 L_1 + \omega_c^2 L_1\right) \tag{39}$$

$$g_v = \frac{2\sqrt{2}k\sqrt{L_1 L_2}\omega_c^8}{\pi\omega_v^4\left(\frac{\omega_v^6 k^2 L_1}{\omega_v^2 - \omega_c^2} - \frac{\omega_v^4 k^2 L_1}{\omega_c^2} - \omega_v^2 L_1 + \omega_c^2 L_1\right)}\cos\frac{\theta}{2}. \tag{40}$$

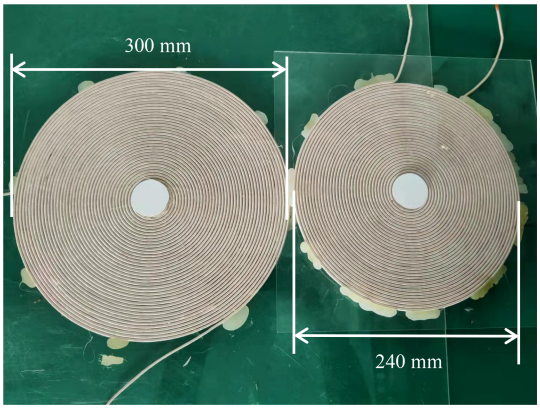

Fig. 13. Experimental platform for double-sided LCC IPT converter.

TABLE I
PARAMETER OF THE PRIMARY AND SECONDARY COIL

Parameter	value
Lize wire (strand diameter, number of strand)	0.1 mm, 500
Diameter and turns number of the transmitter winding	240 mm*240 mm, 32
Diameter and turns number of the receiver winding	300 mm*300 mm, 41
Air Gap	90–120 mm
Self-inductance L_1 at transmitter	208 μH
Self-inductance L_2 at receiver	128 μH
Coupling coefficient	0.13-0.2

TABLE II
ELECTRICAL PARAMETER OF THE PROPOSED SYSTEM

Parameter	value
Input voltage, U_{in}	15 V
Range of load, R_L	0–200 Ω
Output voltage, U_o	59 V
Output current, I_o	1.1 A

IV. RESULTS AND DISCUSSION OF SIMULATION AND EXPERIMENT

As the misalignment-tolerant characteristic of the presented system is investigated, the conventional circular coil is adopted. Fig. 13 shows the coils at the transmitter and receiver and Table I depicts the parameters of coils. This article focuses on the correctness and feasibility of the proposed method. Consequently, the load is replaced with a variable resistance and electric parameters of the proposed system is depicted in Table II. According to the above-mentioned design procedure, other parameters can be determined assuming $k_{\min} = 0.13$ and $k_{\max} = 0.2$, as shown in Table III.

According to the analysis in the previous section, it is clear that owing to maintaining the MOSFETs $S_{c,d}$ ON in the CC output procedure, the current bypasses C_{X2}, and owing to maintaining the MOSFETs $S_{a,b}$ ON in the CV output procedure, the current bypasses C_{X1}. As a result, based on Tables I and II, assuming $C_{X1} = 0$ and $C_{X2} = 0$, the output current and output voltage as the function of the operating frequency are shown in Figs. 14 and 15 under different coupling coefficient and load, where $R = 5\ \Omega$. As clearly shown in Fig. 14(a), the output current is independent

TABLE III
COMPENSATION NETWORK PARAMETERS

Symbols	Parameters	Value
L_{f1}	Primary Compensation Inductor	12.7 μH
C_{f1}	Primary Parallel Capacitor	305 nF
C_1	Primary Series Capacitor	20 nF
C_{X1}	Switched-controlled Capacitor	40 nF
L_{f2}	Secondary Compensation Inductor	31 μH
C_{f2}	Secondary Parallel Capacitor	101 nF
C_2	Secondary Series Capacitor	43 nF
C_{X2}	Switched-controlled Capacitor	40 nF
f_c	Operating Frequency in CC Mode	81 kHz
f_v	Operating Frequency in CV Mode	90 kHz

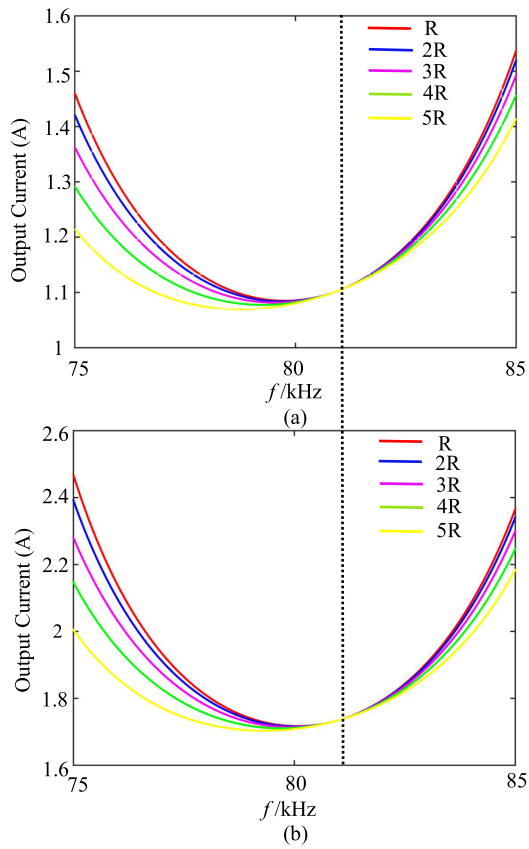

Fig. 14. Output current of the double-sided LCC compensation topology for various load under different coupling coefficient. (a) $k = 0.13$. (b) $k = 0.2$.

of the load at 81 kHz. Further, comparing Fig. 14(a) with (b), the resonant frequency is constant 81 kHz whether $k = 0.13$ or $k = 0.2$. This means that characteristics in (10) and (11) are implemented in the CC output procedure. Furthermore, similar conclusions are drawn from Fig. 15 that the almost constant output voltage is implemented at the operating frequency f_v (90 kHz) regardless of the load, and the resonant frequency is unaffected by the coupling coefficient. This means that characteristics in (13) and (14) are implemented in the CV output procedure.

The input impedance angle of CC and CV output procedures as the function of the coupling coefficient with different C_{1eq} and C_{2eq} are shown in Fig. 16, where $C_{1eq} = C_1 // \pi C_{X1} / [2\pi - 2\beta_c + \sin(2\beta_c)]$ and $C_{2eq} = C_2 // \pi C_{X2}/[2\pi - 2\beta_v + \sin(2\beta_v)]$.

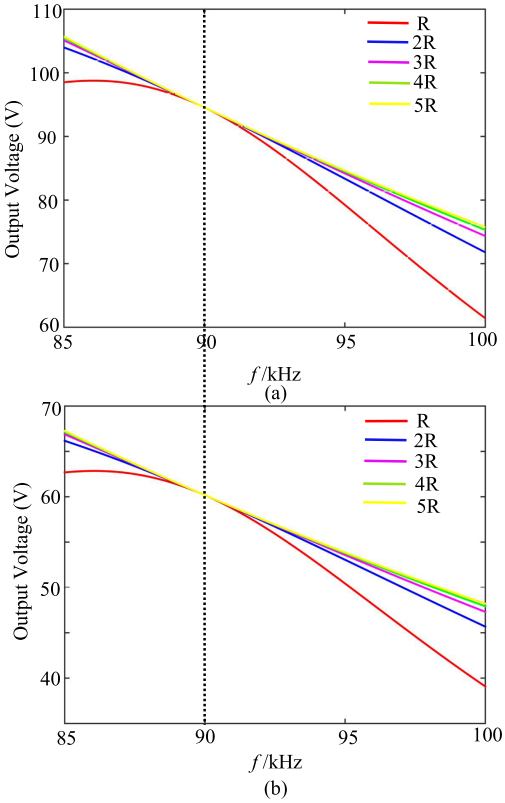

Fig. 15. Output voltage of the double-sided LCC compensation topology for various load under different coupling coefficient. (a) $k = 0.13$. (b) $k = 0.2$.

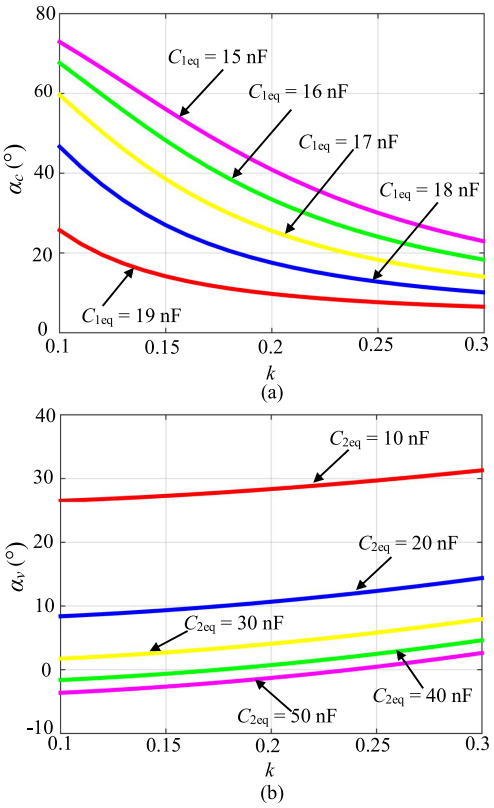

Fig. 16. Input impedance angle various coupling coefficient under different modes. (a) CC mode. (b) CV mode.

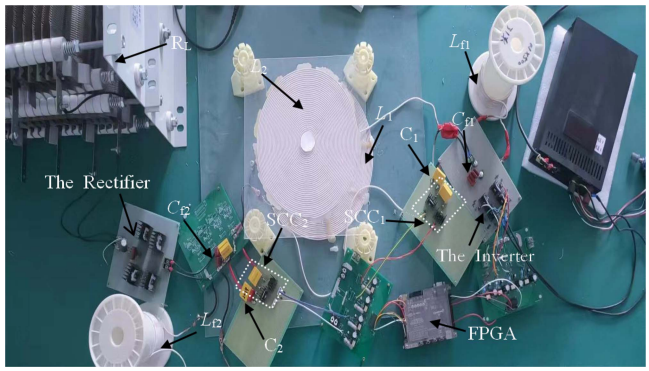

Fig. 17. Experimental platform for double-sided LCC IPT converter.

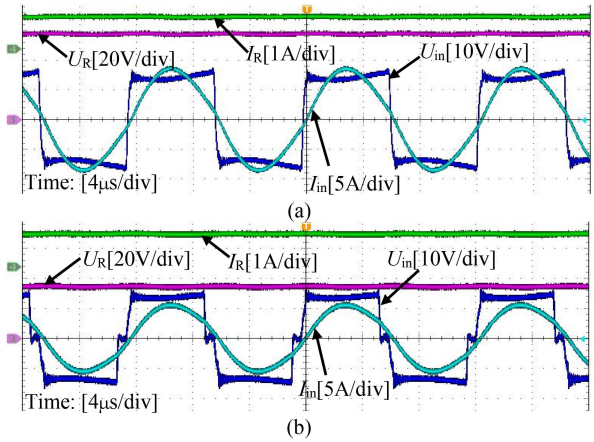

Fig. 18. Experimental waveforms of the output current, output voltage, input current, and input voltage in CC procedure with different load under $k = 0.13$. (a) $R_L = 55\ \Omega$. (b) $R_L = 33\ \Omega$.

Several conclusions can be drawn from Fig. 16(a) and (b). At first, with the coupling coefficient increasing, the variation of impedance angle cannot be ignored whether in the CC output procedure or the CV output procedure. Second, for the same coupling coefficient, the impedance angle of CC and CV output procedures steadily increases as C_{1eq} and C_{2eq} decrease. Thus, by modifying C_{X1} in the CC output procedure while by adjusting C_{X2} in the CV output procedure, soft switching is enabled under different coupling coefficients.

As depicted in Fig. 17, a prototype of 60 W has been constructed to verify the validity and feasibility of the proposed double-sided LCC IPT converter. Here, four MOSFETs (SPW47N60C3) comprise the primary dc–ac full-bridge inverter, while four fast-recovery diodes with manufacturer part number MUR860T make up the secondary rectifier. The ALTBRA EPCE10F17C8N FPGA is employed to implement all the closed-loop control. The switches of SCC are also MOSFETs with manufacturer part number SPW47N60C3.

The experimental waveforms of the proposed converter in the CC output procedure are shown in Figs. 18–21. Comparing Fig. 18(a) with (b), under $k = 0.13$, when the load R_L changes from 55 to 33 Ω, the load current I_R nearly maintain constant at 1.10 A only with the 5° variation of the phase shift angle. Also,

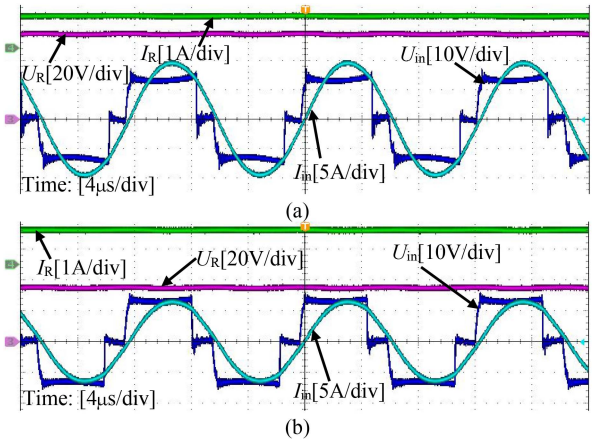

Fig. 19. Experimental waveforms of the output current, output voltage, input current, and input voltage in CC procedure with different load under $k = 0.2$. (a) $R_L = 55\ \Omega$. (b) $R_L = 33\ \Omega$.

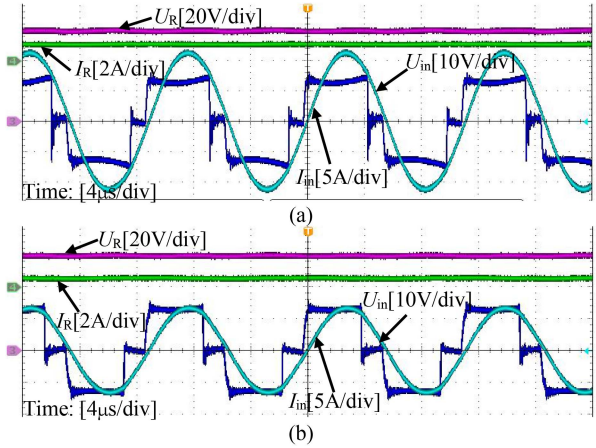

Fig. 22. Experimental waveforms of the output current, output voltage, input current and input voltage in CV procedure with different load under $k = 0.13$. (a) $R_L = 55\ \Omega$. (b) $R_L = 110\ \Omega$.

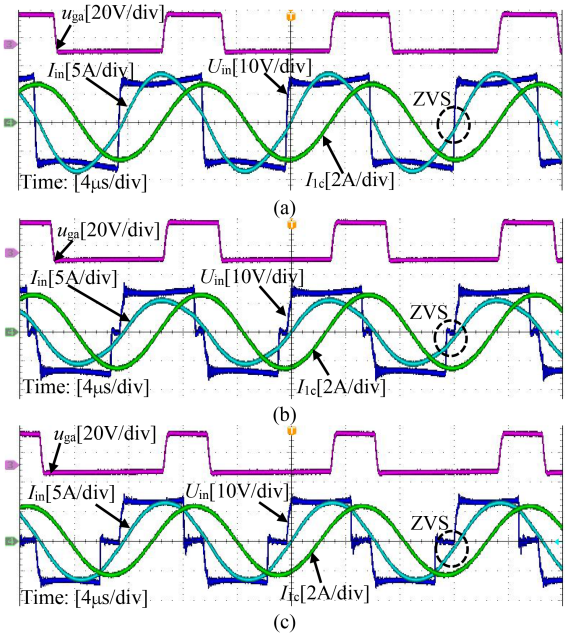

Fig. 20. Experimental waveforms of u_{ga}, $\boldsymbol{I_{1c}}$, input current and input voltage in CC procedure under different load and coupling coefficient. (a) $R_L = 55\ \Omega$, $k = 0.13$. (b) $R_L = 33\ \Omega$, $k = 0.13$. (c) $R_L = 33\ \Omega$, $k = 0.2$.

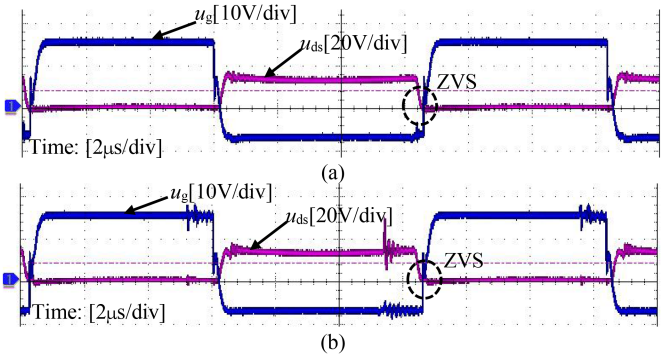

Fig. 21. Experimental waveforms of MOSFET S_4 at $R_L = 55\ \Omega$ and different coupling coefficients in the CC procedure. (a) $k = 0.13$. (b) $k = 0.2$.

from Fig. 19(a) and (b), the same conclusion can be obtained under $k = 0.2$. Moreover, it can be deduced from Figs. 18(a) and 19(a) that when the coupling coefficient k is changed from 0.13 to 0.2, the output current remains 1.10 A by adjusting the phase shift angle from 0° to 27° and the operating frequency f_c (81 kHz) maintain constant independent of the coupling coefficient.

It can be deduced from Fig. 20(a) and (b) that under $k = 0.13$, when the load R_L is changed from 55 to 33 Ω, ZVS with the minimum turn-OFF peak current can be kept by regulating the associated control angle β_c from 133° to 93°. Contrast Fig. 20(b) and (c), under $R_L = 33\ \Omega$, when the variation of k is from 0.13 to 0.2, ZVS under the minimum reactive current can also be maintained by adjusting β_c from 117° to 133°. From Fig. 20(a)–(c), the phasor of the current $\boldsymbol{I_{1c}}$ flowing SCC_1 maintains a constant unaffected by the load and the coupling coefficient. Fig. 21 shows that experimental waveforms of MOSFET S_4 at $R_L = 55\ \Omega$ and different coupling coefficients in the CC procedure. From Fig. 21, ZVS can be implemented at different coupling coefficients. Consequently, SCC can be adopted to regulate the input impedance for ZVS in the CC procedure.

As depicted in Figs. 22–25, the experimental waveforms of the presented double-sided LCC IPT converter during the CV procedure are shown. From Fig. 22(a) and (b), the load voltage U_R maintains constant at 59 V when the load R_L is 55 Ω and 110 Ω, respectively. Comparing Figs. 22(a) with 23(a), some conclusions can be derived. At first, the output voltage at the coupling coefficient $k = 0.13$ remains nearly the same as that at $k = 0.2$ by adjusting the phase shift angle θ from 0° to 33°. Second, it can be found that the operating frequency remains 90 kHz regardless of the coupling coefficient and load.

It is deduced from Fig. 24(a) and (b) that under $k = 0.2$, when the load varies from 55 to 110 Ω, ZVS with the minimum turn-OFF peak current is implemented by modifying the associated control angle β_v of SCC_2 from 137° to 116°. Contrast Fig. 24(b) and (c), ZVS under the minimum reactive current can also be implemented by regulating β_v from 116° to 91° at $R_L = 33\ \Omega$, when k varies from 0.2 to 0.13. As shown in

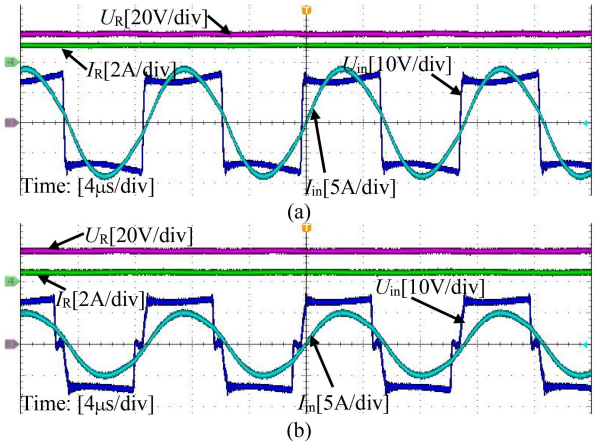

Fig. 23. Experimental waveforms of the output current, output voltage, input current and input voltage in CV procedure with different load under $k = 0.2$. (a) $R_L = 55\ \Omega$. (b) $R_L = 110\ \Omega$.

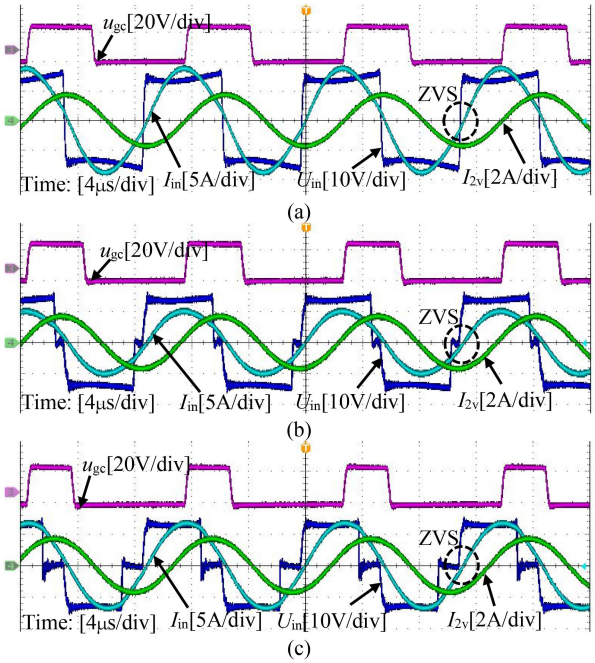

Fig. 24. Experimental waveforms of u_{gc}, $\boldsymbol{I_{3v}}$, input current and input voltage in CV procedure under different load and coupling coefficient. (a) $R_L = 55\ \Omega$, $k = 0.2$. (b) $R_L = 110\ \Omega$, $k = 0.2$. (c) $R_L = 110\ \Omega$, $k = 0.13$.

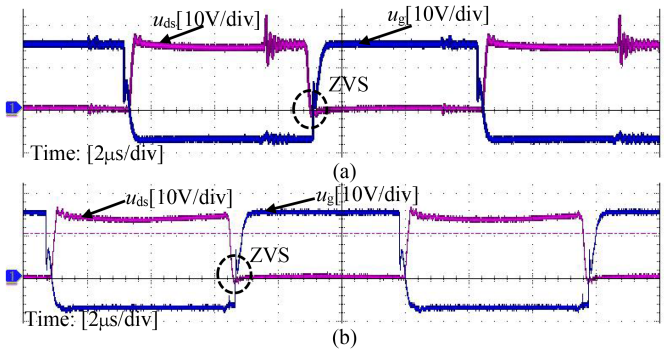

Fig. 25. Experimental waveforms of MOSFET S_4 at $R_L = 55\ \Omega$ and different coupling coefficients in the CV procedure. (a) $k = 0.13$. (b) $k = 0.2$.

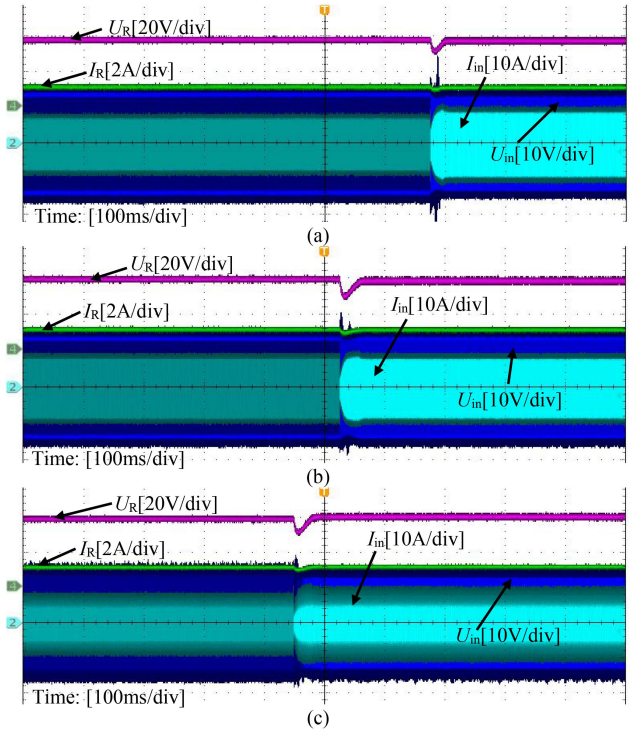

Fig. 26. Experimental waveforms of CC-to-CV transition at different coupling coefficients. (a) $k = 0.13$. (b) $k = 0.17$. (c) $k = 0.2$.

Fig. 24(a)–(c), the phasor of the current $\boldsymbol{I_{3v}}$ flowing SCC_2 maintains constant regardless of the load and coupling coefficient. Fig. 25 shows that experimental waveforms of MOSFET S_4 at $R_L = 55\ \Omega$ and different coupling coefficients in the CV procedure. From Fig. 25, ZVS can be implemented at different coupling coefficients. Thus, in the CV procedure, the SCC could be used to modify the input impedance for ZVS.

Experimental waveforms of CC-to-CV transition at different coupling coefficients are depicted in Fig. 26. Several conclusions can be found from Fig. 26. On the one hand, during the CC-to-CV transition with different coupling coefficients, the output voltage U_R and output current I_R remain almost constant after a transient response time of approximately 20 ms. After the transition from CC to CV, the maximum variation of U_R is 1.6% and that of I_R is 1.7%. On the other hand, at the transition, there is a slight voltage spike caused by the adjustment process of the associated control angle β_v.

Fig. 27 depicts the measured charging profile of output current I_R and output voltage U_R data at different loads. From Fig. 27(a), at $k = 0.13$, maximum variations of the output current in the CC output procedure and output voltage in the CV output procedure are 0.5% and 0.7%, respectively. From Fig. 27(b), at $k = 0.2$, maximum variations of the output current in the CC output procedure and output voltage in the CV output procedure are 0.6% and 1.0%. Therefore, two constant output procedures can be implemented in the proposed IPT system.

Fig. 28 depicts that the dc–dc efficiency at different coupling coefficients and loads in both two output procedures. It can be noticed that at the constant coupling coefficient, with the load

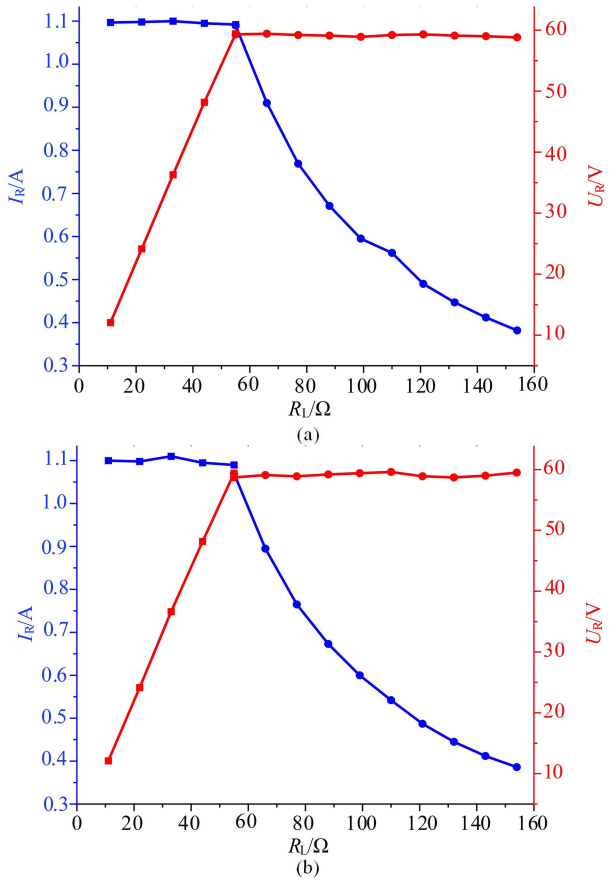

Fig. 27. Measured charging process versus the equivalent load. (a) $k = 0.13$. (b) $k = 0.2$.

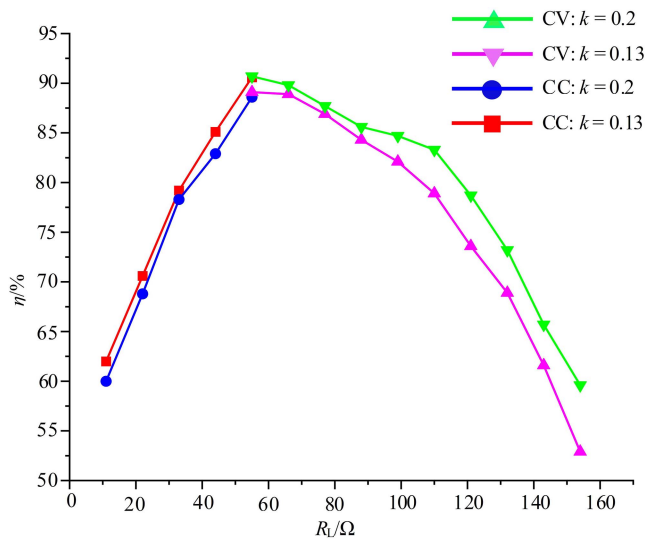

Fig. 28. DC–DC efficiency at different coupling coefficients and loads.

increasing, the efficiency increases in the CC output procedure, while that decreases in the CV output procedure. The peak efficiency in the CC output procedure is 90.6% under $k = 0.13$ and the load $R_L = 55\ \Omega$. Due to the requirement to achieve ZVS with the minimum turn-OFF peak current at different phase shift angles, the reactive current increases at other coupling coefficients, resulting in an efficiency lower than that at $k = 0.13$. The peak efficiency in the CV mode is 90.7% under $k = 0.2$ and the load $R_L = 55\ \Omega$. Owing to the same reason, the efficiency at other coupling coefficients is lower than that at $k = 0.2$.

V. Conclusion

In this article, a novel design approach with SCC control and phase shift modulation of the double-sided LCC compensation circuit is proposed. With the proposed method, during wide load and coupling coefficient range, the double-sided LCC compensated IPT system can implement CC and CV output procedures by regulating the phase shift angle θ and ZVS with minimum reactive current is implemented by modifying the associated control angle of SCC. One of the most significant advantages is that the SCC can be adopted without any phase detection circuit, since the phasor of the current flowing through SCC in two output procedures is not affected by the coupling coefficient and load. Another additional benefit is that whether in CC or CV output procedure, the proposed IPT converter can be operated at an almost fixed frequency, which is beneficial for simplifying the controller and improving the stability of the system. The excellent behavior of the proposed system with respect to a stable operation has been verified by experimental results.

References

[1] Z. Zhang, H. Pang, A. Georgiadis, and C. Cecati, "Wireless power transfer—An overview," *IEEE Trans. Ind. Electron.*, vol. 66, no. 2, pp. 1044–1058, Feb. 2019.

[2] Z. Zhang and K. T. Chau, "Homogeneous wireless power transfer for move-and-charge," *IEEE Trans. Power Electron.*, vol. 30, no. 11, pp. 6213–6220, Nov. 2015.

[3] J. Deng, W. Li, T. D. Nguyen, S. Li, and C. C. Mi, "Compact and efficient bipolar coupler for wireless power chargers: Design and analysis," *IEEE Trans. Power Electron.*, vol. 30, no. 11, pp. 6130–6140, Nov. 2015.

[4] S. Jeong, Y. J. Jang, D. Kum, and M. S. Lee, "Charging automation for electric vehicles: Is a smaller battery good for the wireless charging electric vehicles ?," *IEEE Trans. Autom. Sci. Eng.*, vol. 16, no. 1, pp. 486–497, Jan. 2019.

[5] M. Schormans, V. Valente, and A. Demosthenous, "Practical inductive link design for biomedical wireless power transfer: A tutorial," *IEEE Trans. Biomed. Circuits Syst.*, vol. 12, no. 5, pp. 1113–1130, Oct. 2018.

[6] D. Patil, M. K. McDonough, J. M. Miller, B. Fahimi, and P. T. Balsara, "Wireless power transfer for vehicular applications: Overview and challenges," *IEEE Trans. Transp. Electrific.*, vol. 4, no. 1, pp. 3–37, Mar. 2018.

[7] Y. Chen, R. Mai, Y. Zhang, M. Li, and Z. He, "Improving misalignment tolerance for IPT system using a third-coil," *IEEE Trans. Power Electron.*, vol. 34, no. 4, pp. 3009–3013, Apr. 2019.

[8] R. Mai, B. Yang, Y. Chen, N. Yang, Z. He, and S. Gao, "A misalignment tolerant IPT system with intermediate coils for constant-current output," *IEEE Trans. Power Electron.*, vol. 34, no. 8, pp. 7151–7155, Aug. 2019.

[9] Y. Chen et al., "A hybrid inductive power transfer system with misalignment tolerance using Quadruple-D quadrature pads," *IEEE Trans. Power Electron.*, vol. 35, no. 6, pp. 6039–6049, Jun. 2020.

[10] W. Zhao, X. Qu, J. Lian, and C. K. Tse, "A family of hybrid IPT couplers with high tolerance to pad misalignment," *IEEE Trans. Power Electron.*, vol. 37, no. 3, pp. 3617–3625, Mar. 2022.

[11] L. Zhao, D. J. Thrimawithana, U. K. Madawala, A. P. Hu, and C. C. Mi, "A misalignment-tolerant series-hybrid wireless EV charging system with integrated magnetics," *IEEE Trans. Power Electron.*, vol. 34, no. 2, pp. 1276–1285, Feb. 2019.

[12] X. Qu, Y. Yao, D. Wang, S. Wong, and C. K. Tse, "A family of hybrid IPT topologies with near load-independent output and high tolerance to pad misalignment," *IEEE Trans. Power Electron.*, vol. 35, no. 7, pp. 6867–6877, Jul. 2020.
[13] Y. Chen, B. Yang, Z. Kou, Z. He, G. Cao, and R. Mai, "Hybrid and reconfigurable IPT systems with high-misalignment tolerance for constant-current and constant-voltage battery charging," *IEEE Trans. Power Electron.*, vol. 33, no. 10, pp. 8259–8269, Oct. 2018.
[14] Y. Yao, Y. Wang, X. Liu, Y. Pei, D. Xu, and X. Liu, "Particle swarm optimization-based parameter design method for S/CLC-Compensated IPT systems featuring high tolerance to misalignment and load variation," *IEEE Trans. Power Electron.*, vol. 34, no. 6, pp. 5268–5282, Jun. 2019.
[15] J. Mai, Y. Wang, Y. Yao, and D. Xu, "Analysis and design of high-misalignment-tolerant compensation topologies with constant-current or constant-voltage output for IPT systems," *IEEE Trans. Power Electron.*, vol. 36, no. 3, pp. 2685–2695, Mar. 2021.
[16] Y. Yao, Y. Wang, X. Liu, K. Lu, and D. Xu, "Analysis and design of an S/SP compensated IPT system to minimize output voltage fluctuation versus coupling coefficient and load variation," *IEEE Trans. Veh. Technol.*, vol. 67, no. 10, pp. 9262–9272, Oct. 2018.
[17] Y. Wang, J. Mai, Y. Yao, and D. Xu, "Analysis and design of an IPT system based on S/SP compensation with improved output voltage regulation," *IEEE Trans. Ind. Informat.*, vol. 16, no. 5, pp. 3256–3266, May 2020.
[18] B. Yang et al., "Analysis and design of a T/S compensated IPT system for AGV maintaining stable output current versus air gap and load variations," *IEEE Trans. Power Electron.*, vol. 37, no. 5, pp. 6217–6228, May 2022.
[19] V. Vu, D. Tran, and W. Choi, "Implementation of the constant current and constant voltage charge of inductive power transfer systems with the double-sided LCC compensation topology for electric vehicle battery charge applications," *IEEE Trans. Power Electron.*, vol. 33, no. 9, pp. 7398–7410, Sep. 2018.
[20] J. Lu, G. Zhu, D. Lin, S. Wong, and J. Jiang, "Load-Independent voltage and current transfer characteristics of high-order resonant network in IPT system," *IEEE J. Emerg. Sel. Topics Power Electron.*, vol. 7, no. 1, pp. 422–436, Mar. 2019.
[21] X. Qu, H. Chu, S. Wong, and C. K. Tse, "An IPT battery charger with near unity power factor and load-independent constant output combating design constraints of input voltage and transformer parameters," *IEEE Trans. Power Electron.*, vol. 34, no. 8, pp. 7719–7727, Aug. 2019.
[22] Y. Liu, U. K. Madawala, R. Mai, and Z. He, "An optimal multivariable control strategy for inductive power transfer systems to improve efficiency," *IEEE Trans. Power Electron.*, vol. 35, no. 9, pp. 8998–9010, Sep. 2020.
[23] K. Zhang, W. Gao, R. Shi, Z. Yan, B. Song, and A. P. Hu, "An impedance matching network tuning method for constant current output under mutual inductance and load variation of IPT system," *IEEE Trans. Power Electron.*, vol. 35, no. 10, pp. 11108–11118, Oct. 2020.
[24] Y. Liu and H. Feng, "Maximum efficiency tracking control method for WPT system based on dynamic coupling coefficient identification and impedance matching network," *IEEE J. Emerg. Sel. Topics Power Electron.*, vol. 8, no. 4, pp. 3633–3643, Dec. 2020.
[25] Z. Zhang, F. Zhu, D. Xu, P. T. Krein, and H. Ma, "An integrated inductive power transfer system design with a variable inductor for misalignment tolerance and battery charging applications," *IEEE Trans. Power Electron.*, vol. 35, no. 11, pp. 11544–11556, Nov. 2020.
[26] C. S. Wong, M. -C. Wong, L. Cao, and K. H. Loo, "Design of high-efficiency inductive charging system with load-independent output voltage and current tolerant of varying coupling condition," *IEEE Trans. Power Electron.*, vol. 36, no. 12, pp. 13546–13561, Dec. 2021.
[27] H. Zhang, Y. Chen, C.-H. Jo, S.-J. Park, and D.-H. Kim, "DC-link and switched capacitor control for varying coupling conditions in inductive power transfer system for unmanned aerial vehicles," *IEEE Trans. Power Electron.*, vol. 36, no. 5, pp. 5108–5120, May 2021.
[28] X. Wang, J. Xu, M. Leng, H. Ma, and S. He, "A hybrid control strategy of LCC-S compensated WPT system for wide output voltage and ZVS range with minimized reactive current," *IEEE Trans. Ind. Electron.*, vol. 68, no. 9, pp. 7908–7920, Sep. 2021.
[29] L. Zhou, R. Mai, S. Liu, J. Yu, Y. Li, and L. Fu, "Minimizing input current of the rectifier of LCC–LCC compensated IPT systems by switch-controlled capacitor for improving efficiency," *IEEE Trans. Ind. Appl.*, vol. 58, no. 1, pp. 1010–1021, Jan./Feb. 2022.
[30] S. Li, W. Li, J. Deng, T. D. Nguyen, and C. C. Mi, "A double-sided LCC compensation network and its tuning method for wireless power transfer," *IEEE Trans. Veh. Technol.*, vol. 64, no. 6, pp. 2261–2273, Jun. 2015.

Xuze Zhang was born in Shaanxi Province, China, in 1994. He received the B.S. degree from Chang'an University University, Xi'an, China, in 2016, and the M.S. degree in electrical engineering from Xi'an University of Technology, Xi'an, China, in 2020. He is currently working toward the Ph.D. degree with the School of Electrical Engineering.

His research interests mainly include wireless power transfer and high frequency resonant converter.

Jingang Li was born in Hebei Province, China, in 1968. He received the B.S. degree from Shaanxi Institute of Mechanics, Shaanxi, China, in 1991, the M.S. and Ph.D. degrees in electrical engineering from Xi'an University of Technology, Xi'an, China in 1998 and 2007, respectively.

Since 1991, he has been to Xi'an University of Technology to take part in his work, where he has been an Associate Professor since 2003. His research interests mainly include high frequency, high efficiency power electronics converter, and control system.

Xiangqian Tong was born in Shaanxi, China, in 1961. He received the B.S. degree from the Shaanxi Institute of Technology, Hanzhong, China, in 1983, the M.S. degree from the Xi'an University of Technology, Xi'an, China, in 1989, and the Ph.D. degree in electrical engineering from Xi'an Jiaotong University, Xi'an, China, in 2006.

In 1989, he was with the Xi'an University of Technology, where he has been a Professor since 2002. His research interests include the application of power electronics in power systems and control of power quality.